공학석사학위논문

Selective Adsorption of Rancid Ingredients in Extra Virgin Olive Oil for Enhancing Thermal Stability

열안정성 향상을 위한 엑스트라 버진 올리브유 산패인자의 선택적 흡착에 관한 연구

2017년 8월

서울대학교 대학원
재료공학부
이 성 우

Selective Adsorption of Rancid Ingredients in Extra Virgin Olive Oil for Enhancing Thermal Stability

열안정성 향상을 위한 엑스트라 버진 올리브유 산패인자의
선택적 흡착에 관한 연구

지도교수 곽 승 엽

이 논문을 공학석사 학위논문으로 제출함
2017년 4월

서울대학교 대학원
재료공학부
이 성 우

이성우의 공학석사 학위논문을 인준함
2017년 6월

위 원 장 장 의 영 (인)
부위원장 곽 승 엽 (인)
위 원 안 철 희 (인)

Abstract

Selective Adsorption of Rancid Ingredients in Extra Virgin Olive Oil for Enhancing Thermal Stability

Sungwoo Lee
Department of Materials Science and Engineering
The Graduate School
Seoul National University

Selective removal of free fatty acid and chlorophyll while maintaining beneficial compounds is essential for expanding the use of extra virgin olive oil (EVOO) to the deep frying. In this work, we increased the thermal stability of EVOO by selective removal of rancid compounds with highly efficient adsorbent, (3-Aminopropyl)trimethoxysilane functionalized mesoporous silica with controlled pore size. The adsorption kinetics of rancid compounds into the mesoporous silica were quantitatively analyzed by Langmuir, pseudo-first and Poltorak model. The highest chlorophyll adsorption efficiency was shown in the pore size at 5.85 nm, suggesting that the interaction between the

silica and the chlorophyll could be optimized at this point. In particular the amine-functionalized mesoporous silica showed drastically improved removal efficiency of FFA than the bare silica. Moreover, beneficial compounds like tocopherol and phytosterol maintained even after adsorptive removal. Based on this results, it is expected to attract the considerable amount of interest toward facile adsorptive refining process of EVOO using pore size controlled and amine-functionalized mesoporous silica

Keywords

Mesoporous silica, Adsorption, Refining, Extra virgin olive oil, Adsorption kinetic, Pore size, Functionalization

Student number: 2015-20851

Contents

1. Introduction

Extra virgin olive oil (EVOO) has become a focus of attention owing to its potential health benefits. As reported from many studies, EVOO is effective against cancer, diabetes, heart disease and osteoporosis due to the low saturation rate with abundant functional compounds. Such health benefits attracted consumer's interest about the healthy diet and increased the consumption of EVOO in worldwide. Despite all these health benefits, EVOO has critical drawbacks in cooking at high temperature due to the low thermal stability problem. It is generally known that EVOO produces toxic gas and harmful compounds while deep frying. Therefore low thermal stability problem limits the usage of EVOO to only for the dressing. For this reason, since long ago there were great demands in the olive oil industry to develop deep frying possible EVOO. However, to the best of our knowledge, thermally stable EVOO has as yet never been developed.

Free fatty acid (FFA) and chlorophyll are the most critical rancid compounds of that induce low thermal stability problem of EVOO. Therefore it is necessary to selectively remove FFA and chlorophyll to increase thermal stability while remaining EVOO's healthy compounds. FFA is the strong prooxidant that has high polarity due to a carboxyl group with a long aliphatic chain. At the high temperature, FFA behaves as radical and result in thermo-

oxidative degeneration of triglyceride. This reaction lowers the smoke point and produces toxic gas. Chlorophyll, a large organic molecule with low polarity, behave as a source of strong prooxidant. In the presence of weak acids, magnesium ion is removed, resulting in degradation from chlorophyll to pheophytin. Chlorophyll derivative, pheophytin behave as the prooxidants, thus decreasing the thermal stability of EVOO.

Attempts to solve the thermal stability problem of EVOO by removing rancid compounds may be mainly classified into two approaches; (1) adsorptive refining, and (2) harsh thermal treatment. Although the latter has success in high removal efficiency of rancid compounds in EVOO, harsh thermal condition adversely removes beneficial compounds like tocopherol and phytosterol. Therefore thermal treatment produces the health benefit lost but thermally stable olive oil. In contrast, adsorptive refining has attracted the considerable amount of attentions due to the selective removal capability. Also, adsorptive removal is regarded as a simple and efficient process for selective removal of rancid compounds. For these reasons, it is imperative to develop the high functional and selective adsorbent for EVOO refining process.

Significant efforts have been devoted developing efficient adsorbent for FFA and chlorophyll removal with the wide range of adsorbents such as silica materials, activated clay, and functional resin. However, such approaches imposed a limitation on the necessary to use adsorbent respectively for FFA

and chlorophyll since both compounds have distinct polarity. For this reason, excessive amount of adsorbent is required to refine EVOO and may result low productive yield due to EVOO loss by adsorbent. Therefore, the development of a multi-functional and high efficient adsorbent capable of removing both FFA and chlorophyll is concurrently is required.

Among a variety of adsorbent, mesoporous silica has long been considered a promising candidate for application in EVOO adsorptive refining because of its high surface area, large pore volume, and controllable pore size property. In particular, by controlling the pore size of mesoporous silica large molecules like chlorophyll are easily entrapped into the mesopore. However, practical usage of bare mesoporous silica in EVOO adsorptive refining appears to be distant due to weak adsorption strength and further surface modification is necessary.

Here in, we are motivated to develop a multi-functional and high-efficient adsorbent for EVOO via pore size-controlled mesoporous silica and amine surface modification. Our adsorbent exhibit not only much higher FFA adsorption efficiency than conventional mesoporous silica but also facilitate to remove both FFA and chlorophyll with the single adsorbent. The results were achieved by entrapment of chlorophyll into porous structure and enhancing interaction between FFA by amine functionality. We especially focused on analyzing pore size effect and surface functionality effect with

various kinetic models. Pore size effect was quantitatively analyzed by Poltorak model with pore size-controlled mesoporous silica. Furthermore, optimal pore size for confining FFA and chlorophyll was investigated. The effect of amine functional group was investigated by Langmuir model. We believe that our multi-functional and high-efficient adsorbent may set new trends and offer unprecedented access to next-generation EVOO refining process.

3. Experimental

2.1. Materials

EVOO and the refined olive oil are obtained from Genesis Co. Ltd, Korea. Three different types of surfactants, Cetrimonium bromide (CTAB, 98%, Alfa Aesar), Pluronic 123 (P123, Mn~5800, Sigma-Aldrich), 1,2,4–Trimethylbenzene (TMB, 98%, Alfa Aesar), were used as the template to control the pore size of the mesoporous silica. Tetraethyl orthosilicate (TEOS, 98%, Sigma-Aldrich) which is a colorless liquid that degrades in water was used as the silica source. Amine functionality was introduced on the silica surface by (3-Aminopropyl)trimethoxysilane (APTMS, 97%, Sigma-Aldrich). Hydrochloric acid (HCl, 37%, Junsei) and NaOH (Granule, Daejung, Korea) were used to make the solution in a proper pH. Remaining surfactants could be removed by Piranha solution which is made by sulfuric acid (H_2SO_4, 97%, PFP), Hydro peroxide (H_2O_2, 35%, Junsei) in a ratio of 7:3. All chemicals were used as received.

2.2. Synthesis of pore size controlled mesoporous silica

Hexagonally ordered mSiO_2-OH (S) was synthesized similarly as procedures reported in the literature. 0.46 g of NaOH granule was dissolved in 120 ml of deionized water at room temperature. After pH was properly balanced by NaOH, 1.4 g of white CTAB powder was added into the solution at 35 °C and vigorously stirred until the murky solution turns to clear solution. When the solution becomes homogeneous, 5.6 ml of TEOS was added dropwise, giving rise to a white slurry. After stirring for 24 h at 35 °C, white precipitants were obtained, and hydrothermal reaction was taken at 100 °C for 72 h. The product was filtered and washed with deionized water and dried under vacuum condition at 60 °C. Lastly, the as-synthesized mSiO_2-OH (S) was calcined in air at 500 °C for 5 h.

Synthesis of mesoporous silica mSiO_2-OH (M) was similar to the method reported previously by Zhao et al. 30 g of 2 M HCl was added to 15 ml of deionized water to control the pH of the solution. After that, 2 g of P123 was fully dissolved in the solution by stirring at 35 °C. When the solution becomes clear, dropwise addition of 4.4 g TEOS was taken. The mixture was stirred for 24 h at 35 °C, and then the hydrothermal reaction was carried at 100 °C for 72 h. The solid was filtered off, washed with deionized water, and calcined at 500 °C for 5 h.

The $mSiO_2$-OH (L) was prepared by the similar procedure of $mSiO_2$-OH (M). 2 g of P123, 52 g H_2O and 10 ml of HCl 35% are stirred fully at 35 °C until the solution becomes clear. After that 2 g of TMB was added and another 24 h stirring was taken to stabilize the microemulsion. When microemulsion was stabilized 4.3 g of TEOS was dropwise added into the solution and another 24 h stirring was taken. After that, the additional hydrothermal reaction was carried in 100 °C for 72 h and filtered before calcination at 500 °C for 5 h.

2.3. Amine-functionalization of mesoporous silica

Remaining surfactants and other impurities left in mesoporous silica particles were removed by reflux process with piranha solution for 24 h at 100 °C. Resulting particles was filtered, washed with deionized water. APTMS functionalization was performed on the silica materials using the post-grafting method. The mixture of 1 g of mesoporous silica and 2 g of APTMS in 50 ml of toluene was refluxed for 24 h at 100 °C with vigorous stirring. The functionalized silica was filtered and washed with toluene.

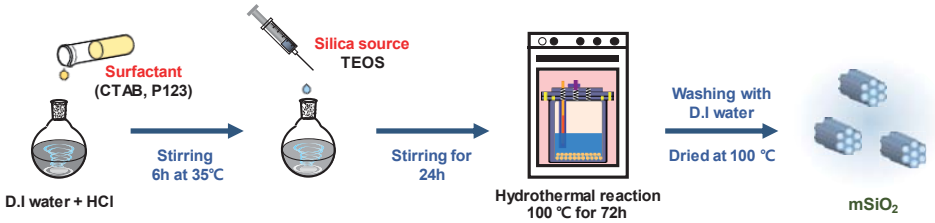

Fig. 1. Synthesis procedures of the mesoporous silica with various surfactants.

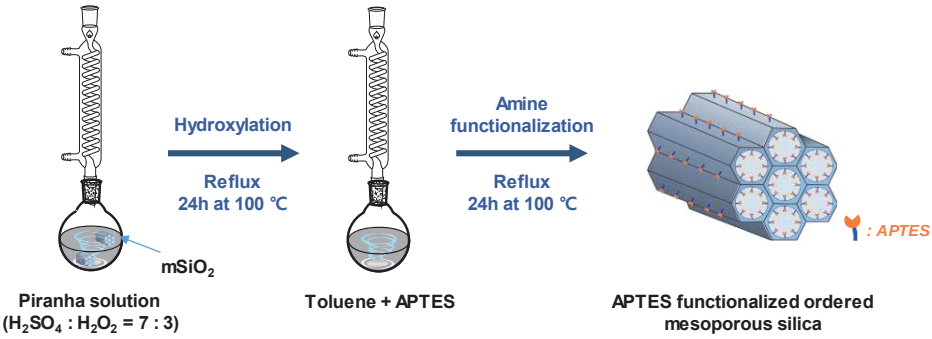

Fig. 2. Procedures of the APTMS functionalization.

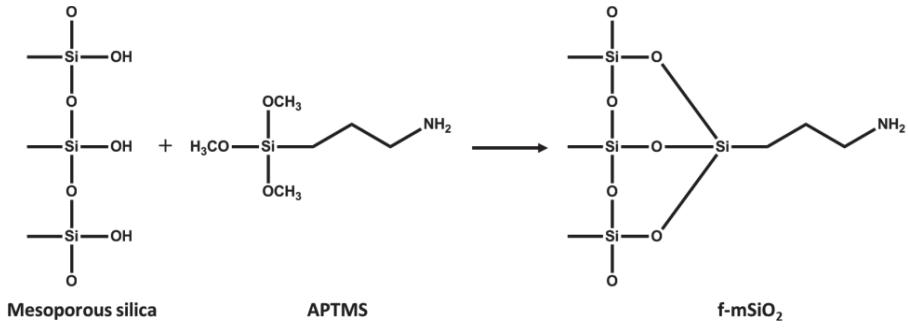

Fig. 3. Schematic diagram of the amine-functionalization.

2.4. Characterization

XRD (X-ray diffraction) measurements were taken with Bruker New D8-Advance using with CuK_{α} radiation (40 KV, 40 mA, $\lambda = 1.5406$ Å) to identify the ordered porous structure of mesoporous silica. N_2 adsorption-desorption isotherms were measured with a 3FLEX Micromeritics at liquid nitrogen temperature. The specific surface area of the samples was calculated by utilizing the Brunauer-Emmett-Teller (BET) method. By using the Barrett-Joyner-Halenda (BJH) model, the pore volumes and pore size distribution curves were obtained. High-resolution transmission electron microscopy (HR-TEM) experiments were conducted using a JEM-3010 microscope operated at 300 KV to observe hexagonally aligned pore structure, and the pore size of ordered mesoporous silica. Field-emission scanning electron microscopy (FE-SEM) was employed to observe the morphology of mesoporous silica particles. Energy-dispersive X-ray spectroscopy (EDX) was also performed to analyze its chemical elemental components. Fourier transform infrared (FT-IR) spectra were collected with Thermo Scientific Nicolet spectrophotometer, using potassium bromide powder. The functionality of ordered mesoporous silica was analyzed by magic angle spinning NMR (MAS NMR, 500MHz Solid NMR Bruker Advance II). The degree of functionalization was calculated by comparing the integral ratio of silanol peaks and APTMS peaks.

2.5. Adsorption kinetics

To determine the surface property effect and pore size effect on adsorption, batch adsorption investigation was taken by agitating silica adsorbent with EVOO in 120 °C and vacuum condition. When the adsorption was finished, the particles were filtered with cellulose filter paper (Advantec, average pore size 0.45 μm).

The measurement of FFA concentration in EVOO was carried out using titration method. For the analysis, 0.2 g of sample is transferred into a conical flask containing 5 g of IPA : Toluene = 1 : 1 solution. The mixture was titrated with 0.01 N NaOH using phenolphthalein as an indicator to determine the unremoved FFA in EVOO. All the experiments were repeated at least three times to check the reproducibility of the obtained results.

The chlorophyll content of EVOO can be determined by the American Oil Chemists' Society (AOCS) method. The transmittance reading at 630, 670, and 710 nm was taken into account with their corresponding coefficients and concentration of chlorophyll was calculated by the following equation. (Eq. 1)

$$\boldsymbol{Chlorophyll, ppm = A_{670} - \left(\frac{A_{630}+A_{710}}{2}\right) \div 0.0964} \qquad (1)$$

(i) Langmuir model: The adsorption characteristics of a solute on the adsorbent

can be studied through the Langmuir isotherm and the equation is expressed as follow (Eq. 2):

$$\frac{q}{q_m} = \frac{K_A X_e}{1+K_A X_e} \quad (2)$$

where X_e (mg) is the amount of adsorbate in solution at equilibrium, q (mg/g) is the amount of adsorbate adsorbed per gram of adsorbent, q_m (mg/g) is the amount the adsorbate adsorbed to form a monolayer coverage and K_A is the Langmuir adsorption equilibrium constant

(ii) Pseudo-first order model: The pseudo-first order adsorption kinetic model is expressed as follow (Eq. 3).

$$q_t = q_{cal}\left(1 - e^{-kt}\right) \quad (3)$$

where k is the adsorption rate constant, which can be determined by plotting q_t versus t. By using the pseudo-first order model, we can derive the theoretical maximum adsorption quantity.

(iii) Poltorak model: The Poltorak equation can be used to determine the adsorption and desorption kinetic constants of the inner pore. The Poltorak model is expressed as follow (Eq. 4).

$$\frac{1}{t} ln \frac{1-a\theta}{1-\theta} = \left(k_a C_0 - \frac{1}{2} k_a k_d C_0 t\right)(1-a) \quad (4)$$

where $\theta = q_t/q_{max}$ and $a = q_{max}/C_0V$. The k_a/k_d quotient can be an actual hint of the final adsorption.

The performance of column is usually evaluated with the concept of breakthrough curve.[32] The breakthrough curve can be obtained by plotting the dimensionless concentration C_t/C_0 versus time or volume of the effluent. The effluent volume, V_{eff} (mL), is calculated from the following equation:

$$V_{eff} = Qt_{total} \quad (5)$$

Total mass of adsorbate, q_{total} (mg), adsorbed at specific column parameters can be calculated from the following equation:

$$q_{total} = \frac{Q}{1000} \int_0^{t_{total}} C_{ad} dt = \frac{Q}{1000} \int_0^{t_{total}} (C_0 - C_t) dt \quad (6)$$

where Q is the volumetric flow rate (mL/min), t_{total} is the total flow time (min), C_{ad} is the adsorbed adsorbate concentration (mg/L). The integral in above

equation is equal to the area in the breakthrough curve. Maximum capacity of the column or equilibrium adsorbate uptake per unit mass of adsorbent, $q_{eq(exp)}$ (mg/g), is calculated as following:

$$\boldsymbol{q_{total}} = \frac{\boldsymbol{q_{total}}}{\boldsymbol{M}} \tag{7}$$

where M is the dry weight of adsorbent packed in the column (g). Total amount of adsorbate passing from the column (m_{total}) and total removal percentage of adsorbate (Y%) are calculated from the following equation:

$$\boldsymbol{m_{total}} = \frac{\boldsymbol{C_0 Q t_{total}}}{\mathbf{1000}} \tag{8}$$

$$\mathbf{Y}(\%) = \frac{\boldsymbol{q_{total}}}{\boldsymbol{m_{total}}} \times \mathbf{100} \tag{9}$$

3. Results and Discussion

3.1. Characteristics of ordered mesoporous silica

3.1.1 Ordered porous structure of mesoporous silica

The wide angle X-ray diffraction (XRD) patterns of the ordered mesoporous silica were analyzed to investigate the effects of NaOH on the arrangement of mesopores. Fig. 4 shows the XRD patterns of mSiO_2-OH (S) prepared at 100 °C using gels with different NaOH amount. When NaOH was added above 4.3 g, d_{110} peak intensity was stronger than d_{100} peak intensity. This result implies the presence of amorphous pore structure. However, the intensity of the diffraction peak became stronger and better resolved as less NaOH was added. At the specific synthesis condition, 0.34 g NaOH, all d_{100}, d_{110}, d_{200} peaks could be examined. This result indicates the existence of an optimal pH value for the ordered porous structure and when 0.34 g of NaOH was added mesopores were periodically ordered. Besides, as less NaOH was added the d_{100} peak shifted to the lower angle and this implies the increase of pore size.

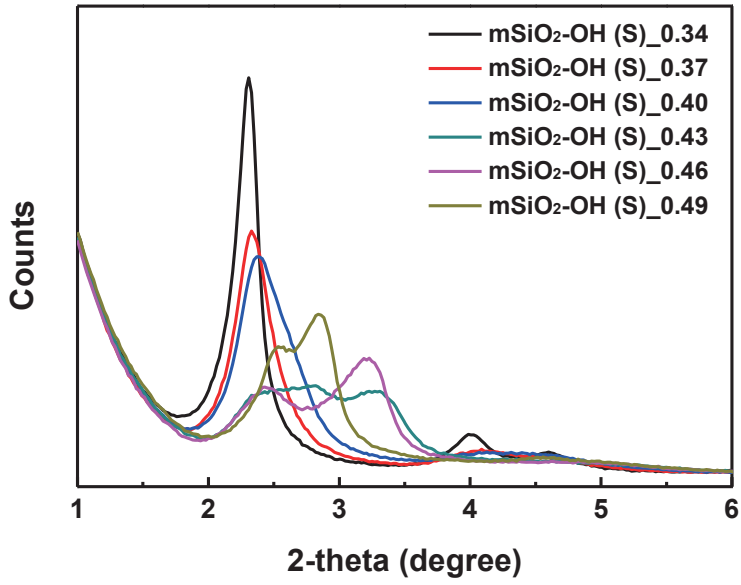

Fig. 4. XRD patterns of $mSiO_2$-OH (S) made from gels with different amount of NaOH

Table 1. Synthesis condition and sample code.

NaOH	Temperature	Sample code
0.34	100 °C	mSiO$_2$-OH_0.34
0.37	100 °C	mSiO$_2$-OH_0.37
0.40	100 °C	mSiO$_2$-OH_0.40
0.43	100 °C	mSiO$_2$-OH_0.43
0.46	100 °C	mSiO$_2$-OH_0.46
0.49	100 °C	mSiO$_2$-OH_0.49

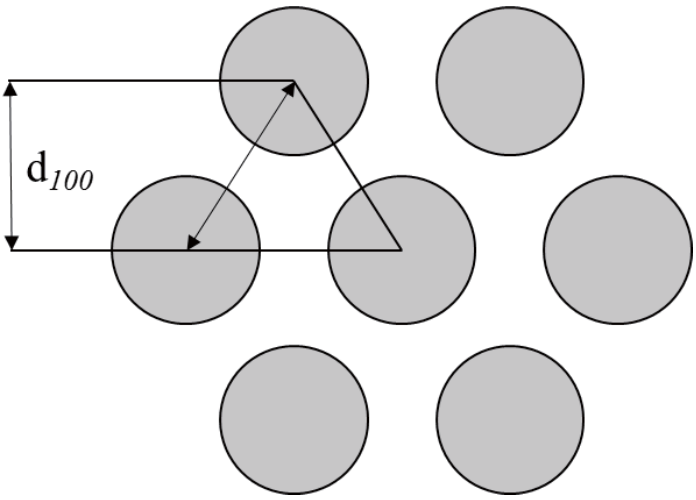

Fig. 5. Schematic illustration of a hexagonal structure with the d_{100} spacing and unit cell parameter a

The influence of hydrothermal temperature on the $mSiO_2$-OH (M) was investigated. XRD peak shifted to the lower angle as temperature increased and peak shifting indicates a pore size change. The pore size can be approximately calculated using the following primary mesopore diameter equation:

$$w_d = cd_{100}\left(\frac{\rho V_p}{1+\rho V_p}\right)^{1/2} \quad (10)$$

where c is a circular pore constant, $(8/3^{1/2}\pi)^{1/2}$, d_{100} is an interplanar distance, ρ is a pore wall density (2.2 g/cm^3) and V_p is the primary mesopore volume. Fig. 6 shows the XRD patterns of $mSiO_2$-OH (M) prepared with different hydrothermal temperature condition. When hydrothermal temperature increases, d_{100} peak shifted to the lower 2-theta. This result implies the increase of pore diameter. The pore diameter calculated by XRD increased from 4.9 nm to 5.5 nm with increasing the hydrothermal temperature from 80 °C to 120 °C.

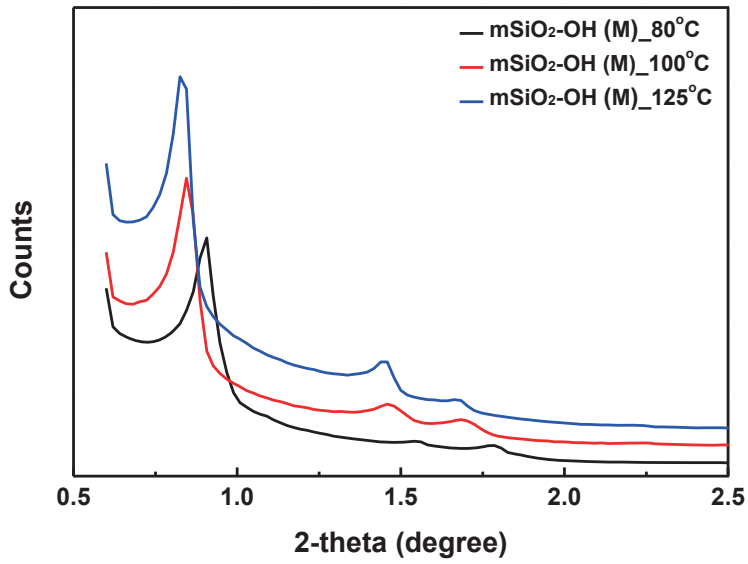

Fig. 6. XRD patterns of $mSiO_2$-OH (M) synthesized by different hydrothermal temperature.

Table 2. Synthesis condition and pore diameter

Sample code	Temperature	Pore size
$mSiO_2$-OH_(M)_80 °C	80 °C	4.9 nm
$mSiO_2$-OH_(M)_100 °C	100 °C	5.3 nm
$mSiO_2$-OH_(M)_120 °C	120 °C	5.5 nm

Nitrogen adsorption-desorption isotherms are shown in Fig. 7. $mSiO_2$-OH (M) and $mSiO_2$-OH (L) yields an isotherm (type IV) with H_1-type hysteresis that is typical of mesoporous materials with 1D cylindrical channels. Steep condensation steps represent a high uniformity of mesopores. From the BET isotherm, the structure of mesoporous could be verified. $mSiO_2$-OH (S) had the BET pattern of type IV with very small hysteresis, indicating that its pore size is slightly above 2 nm. The pore size distributions of the mesoporous silica were analyzed by using the BJH method (Fig. 8). The average pore diameter of ordered mesoporous silica determined by BJH plot are 2.4 nm, 5.5 nm and 10.5 nm. Physical parameters, surface area and pore size, for the ordered mesoporous silica series are given in Table 3.

The TEM images (Fig. 9) showed that all three ordered mesoporous silica had a hexagonal shape with a regular arrangement of pores. HR-TEM images shows that all three samples had well-ordered hexagonal arrays of mesopores with one-dimensional pore channels. From the HR-TEM image verified that mesoporous silica having 2-D hexagonal (P6mm) mesostructure.

Table 3. Physical properties of ordered mesoporous silica

Sample	Pore diameter	Surface area
$mSiO_2$-OH_(S)	2.4 nm	963 m^2g^{-1}
$mSiO_2$-OH_(M)	5.5 nm	514 m^2g^{-1}
$mSiO_2$-OH_(L)	10.5 nm	395 m^2g^{-1}

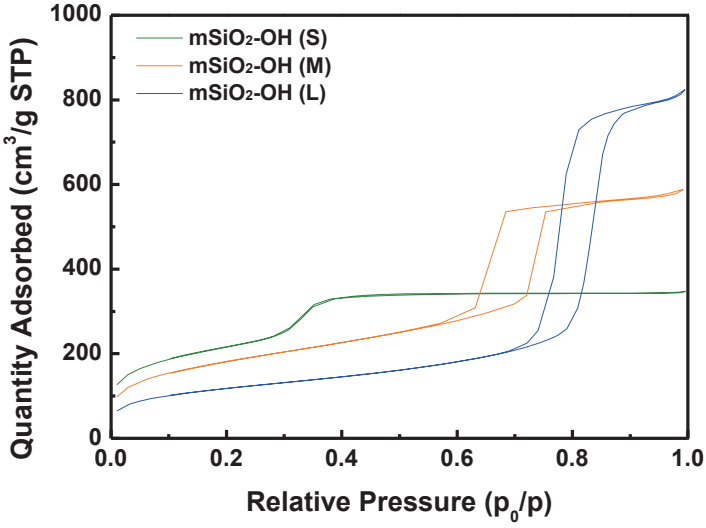

Fig. 7. Nitrogen gas (N_2) adsorption-desorption isotherm

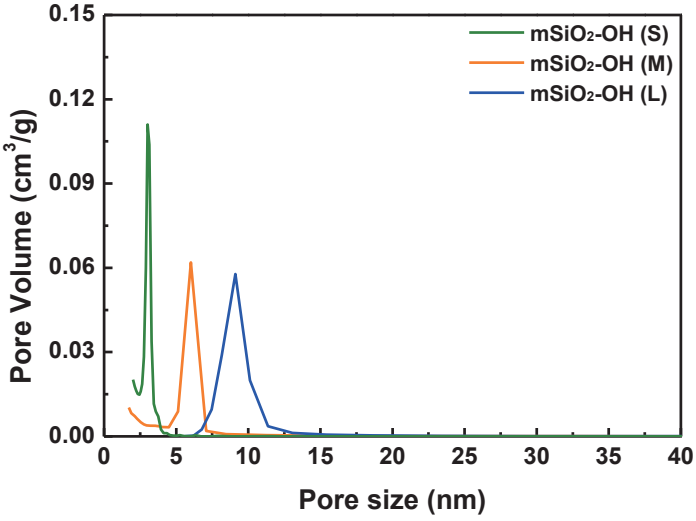

Fig. 8. Barrett-Joyner-Halenda (BJH) plot of ordered

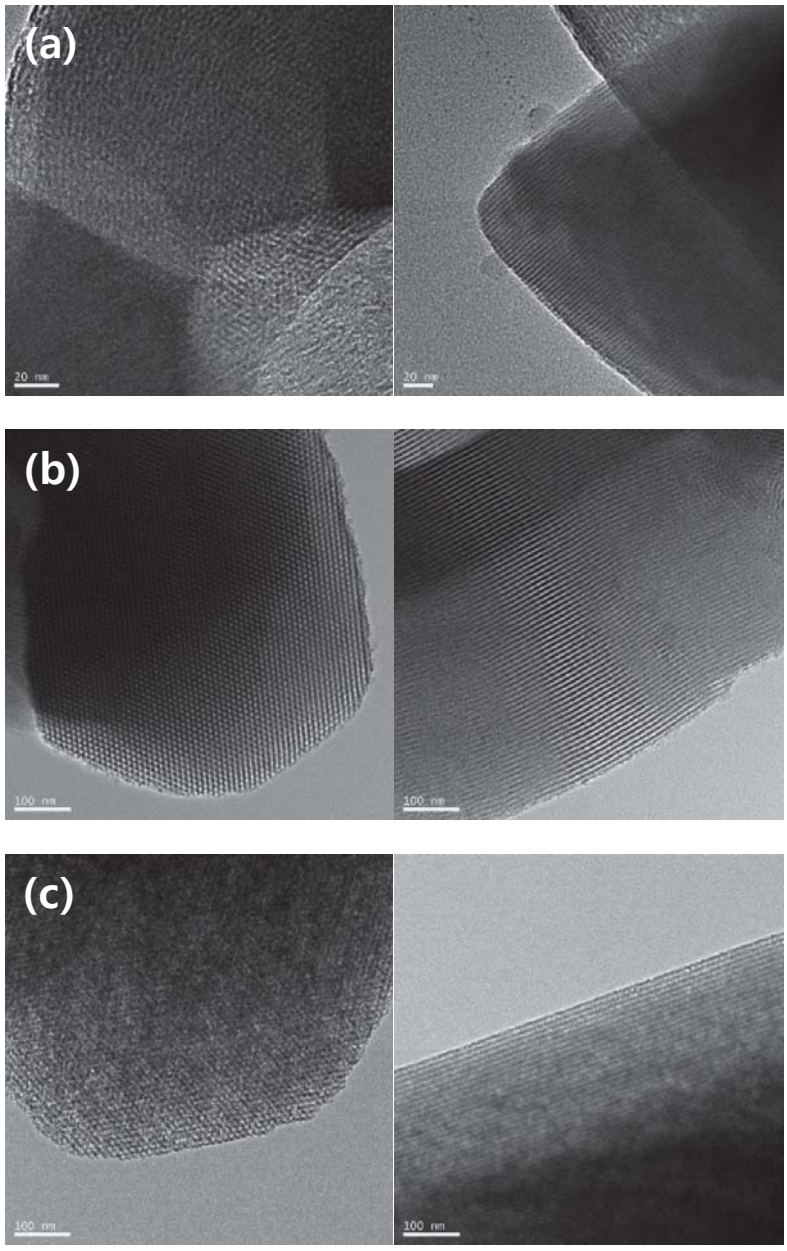

Fig. 9. (a)Nitrogen gas (N_2) adsorption-desorption isotherm; (b) Barrett-Joyner-Halenda (BJH) plot of ordered mesoporous silica

3.2. Characteristics of functionalized mesoporous silica

3.2.1 Structural propoerties

To investigate the surface area and pore size distribution, nitrogen adsorption-desorption analysis was taken. BET results of the ordered mesoporous silica are presented in Fig. 10. The BET patterns show that $mSiO_2$-NH_2 (S) is type I with the characteristic plateau with a small hysteresis, indicating that its pore size is around 2 nm. $mSiO_2$-NH_2 (M) and $mSiO_2$-NH_2 (L) are showing the type IV curves with characteristic hysteresis loops. Both isotherms exhibited very steep condensation steps with narrow width, which reflect a high uniformity of mesopores. The pore size distributions of the mesoporous silica were analyzed by using the BJH method. As shown in Fig. 11, the average pore diameters of ordered mesoporous silica determined by BJH plot are 2.01 nm, 5.85 nm, and 8.76 nm. Due to the limitation of analysis instrument, the BJH curve of $mSiO_2$-NH_2 (S) was partially plotted. However, it seems clear that pore structure of $mSiO_2$-NH_2 (S) was maintained even after amine functionalization. To verify this supposition we conducted XRD analysis

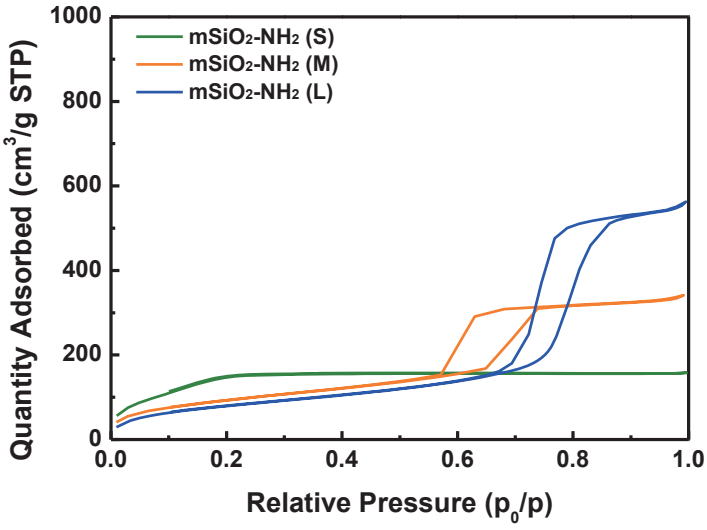

Fig. 10. Nitrogen gas (N_2) adsorption-desorption isotherm of amine-functionalized mesoporous silica

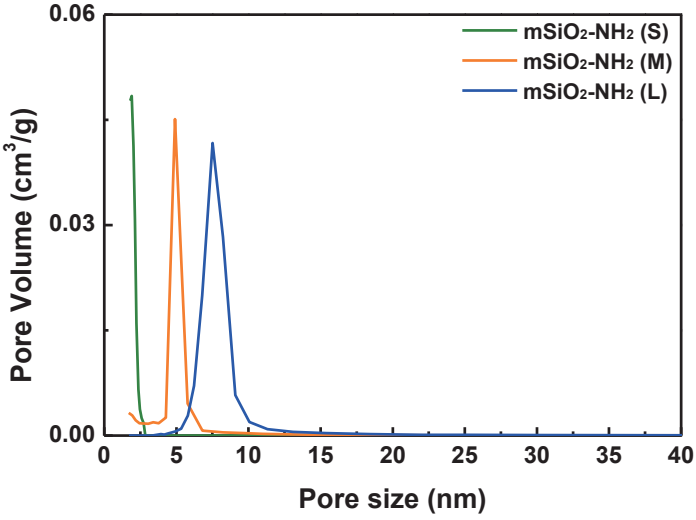

Fig. 11. Barrett-Joyner-Halenda (BJH) plot of amine-functionalized mesoporous silica

Table 4. Pore structure parameters of mesoporous silica adsorbent

Sample	Average surface area	Average pore diameter
$mSiO_2$-NH_2_(S)	506 m^2g^{-1}	2.01 nm
$mSiO_2$- NH_2_(M)	333 m^2g^{-1}	5.85 nm
$mSiO_2$- NH_2_(L)	338 m^2g^{-1}	8.76 nm

The XRD patterns were analyzed to investigate the hexagonally ordered cylindrical pore structure of the ordered mesoporous silica. The XRD patterns in each sample exhibited a strong (100) peak and weak additional peaks, which can be indexed as (110) and (200) reflections in a hexagonal lattice. Specific peaks of ordered mesoporous silica observed by XRD confirmed 2-D hexagonal (P6mm) mesostructured with one-dimensional pore channels. The pore size can be approximately

calculated using the following primary mesopore diameter equation:

$$w_d = cd_{100}\left(\frac{\rho V_p}{1+\rho V_p}\right)^{1/2} \quad (10)$$

where c is a constant characteristic of the pore geometry, ρ is a pore wall density (2.2 g/cm^3), and V_p is the primary mesopore volume. The pore diameter calculated by XRD increased from 1.71 nm to 5.67 nm with varying the surfactant template (Fig. 12). As the average pore diameter increased, diffraction peaks shifted toward lower angles indicating that the pore diameters are successfully controlled by the surfactants.

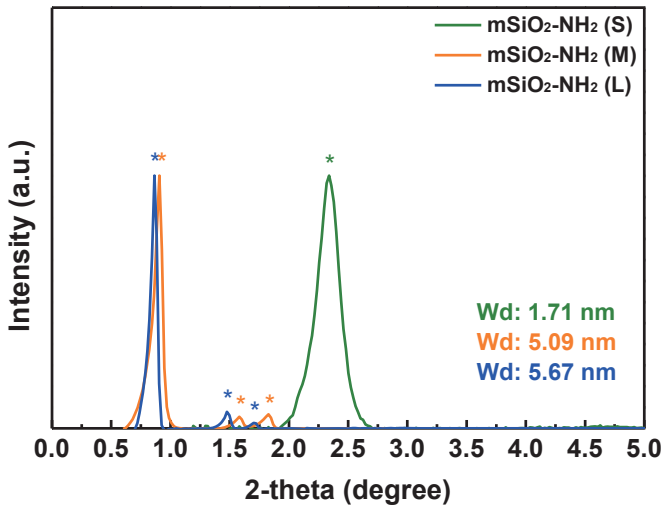

Fig. 12. XRD patterns of $mSiO_2$-NH_2 made from different surfactant

To confirm the arrangement of pores and the pore structure in the visual image, HR-TEM images were obtained as shown in Fig. 13. HR-TEM images of amine-functionalized mesoporous silica confirmed well-ordered hexagonal arrays of mesopore with one-dimensional pore channels indicating a 2-D hexagonal (P6mm) mesostructured. This means that the APTMS functionalized mesoporous silica materials maintained the native structure even after surface functionalization. In addition, the difference in pore size between each sample was apparent in HR-TEM images.

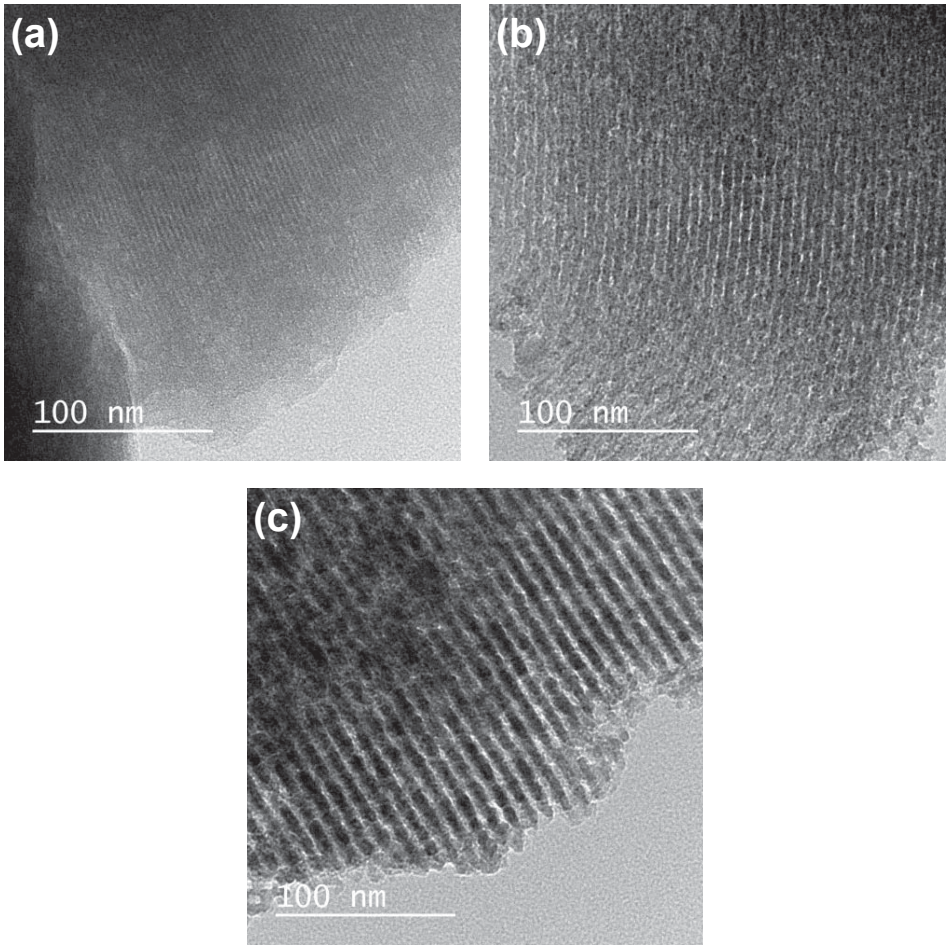

Fig. 13. Transmission electron microscope (TEM) image of (a) $mSiO_2$-NH_2 (S), (b) $mSiO_2$-NH_2 (M) and (c) $mSiO_2$-NH_2 (L)

3.2.2 Surface properties

The FT-IR spectrums of APTMS-functionalized ordered mesoporous silica are illustrated in Fig. 14. The absorbance peaks corresponding to symmetrical and asymmetrical C–H stretching peaks of APTMS appear in the range of 2850–3000 cm^{-1}. Also, peaks at 1494 cm^{-1} is assigned to the bending vibration of C–H of APTMS. The weak absorption at 1563 cm^{-1} that attributed by the bending vibration of NH_2 confirms the incorporation of amino groups. In addition, the significant decrease in the intensity of Si–OH and O–H stretching vibration bands in around 967 cm^{-1} is due to the chemical bond between the surface Si–OH groups of SiO_2 and ethoxy groups of APTMS. The strong peak around 1632 cm^{-1} is mainly of the bending vibration of some physisorbed H_2O molecules. From these results, we could confirm that APTMS successfully incorporated with mesoporous silica adsorbent.

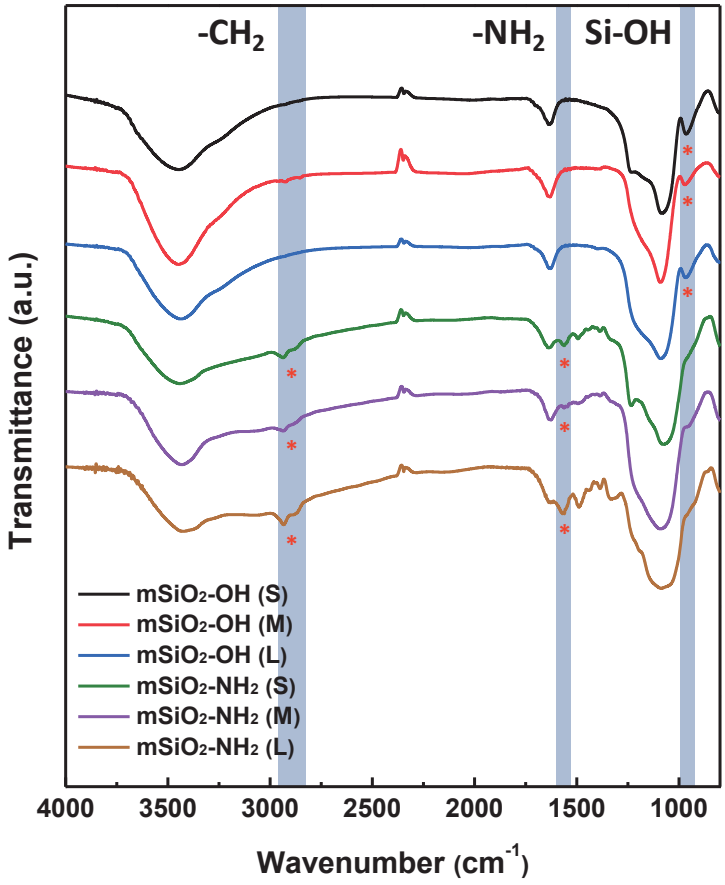

Fig. 14. Fourier transformed infrared (FTIR) spectra of $mSiO_2$-OH and $mSiO_2$-NH_2

Fig. 15 shows the ^{29}Si MAS NMR spectra of the amino group functionalized mesoporous silica and the bare mesoporous silica. Three strong up-field resonance peaks corresponding to Q_4 (–110 ppm), Q_3 (–100 ppm) and Q_2 (–90 ppm) are related to siloxane (Si–O–Si) groups and silanol (Si-OH) groups, $Q_n = Si(OSi)_n(OH)_{4-n}$, n = 2–4. In addition, two down–field peaks assigned to T_3 (–65 ppm) and T_2 (–58 ppm) corresponds to $T_m = RSi(OSi)_m(OH)_{3-m}$, m = 1–3. The appearance of T_m peaks and decrement of Q_n peaks clearly confirms that the aminosilane coupling agents and the silica were successfully incorporated.

As can be seen in Fig. 15, bare mesoporous silica has high Q_3 peak intensity than Q_4 and Q_2 peak. The results are commonly shown to high surface-silica materials such as mesoporous MCM-41 or SBA-1. Therefore we can assume that $mSiO_2$-OH has high surface area.

The ^{29}Si MAS NMR analysis of functionalized mesoporous silica provided more detailed information about the structure integrity of organosilanes on mesoporous silica. By comparing the Q_n and T_m integral area, the degree of functionalization could be compared. All three samples had near 0.5 integral area ratio between Q_n and T_m which indicates that all samples were functionalized in similar degree.

To calculate the degree of functionalization in more detail, the change of

hydroxyl group was confirmed by comparing the peak intensity of Q_n. Total amount of hydroxyl functionality can be assumed by Q_3 and Q_2 peak. Therefore by comparing the Q_n intensity of bare mesoporous silica with Q_n peaks of amine functionalized silica, we can approximately calculate the degree of functionalization.

As can be seen in Table 6, all three samples had near 40%, (OQ_3-Q_3+Q_2) value which indicates that all samples were functionalized in similar degree. This result correspond with the value calculated by comparing integral ratio of Q_n peaks and T_m peaks.

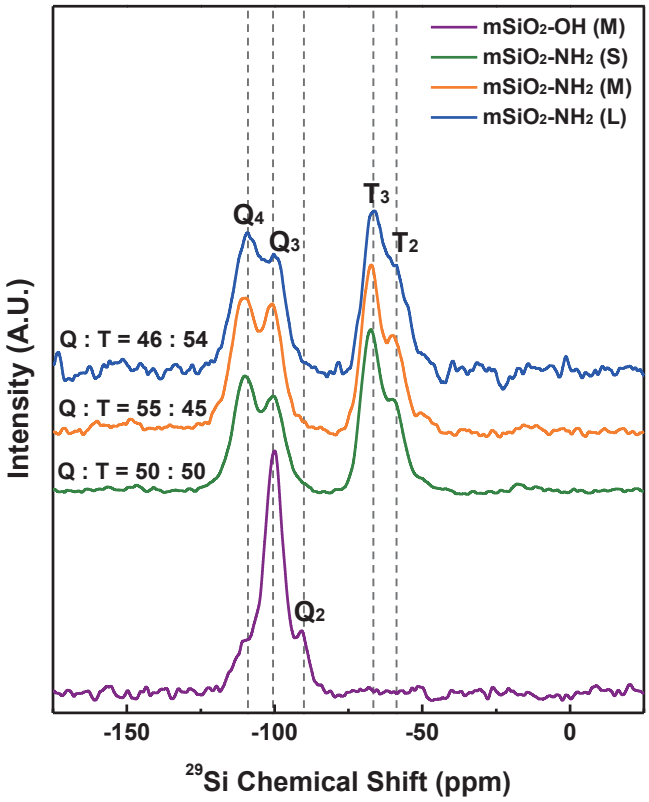

Fig. 15. ^{29}Si MAS NMR of $mSiO_2$-OH (M) and $mSiO_2$-NH_2 (M)

Table 5. Integrated intensities of Q_n and T_m

Sample	$Q_n/(Q_n+T_m)$	$T_m/(Q_n+T_m)$
$mSiO_2$-NH_2 (S)	0.497	0.503
$mSiO_2$- NH_2 (M)	0.550	0.450
$mSiO_2$- NH_2 (L)	0.457	0.543

Table 6. Degree of functionalization calculated by Q_n peak intensity

Sample	$mSiO_2$-OH (M)			$mSiO_2$-NH_2 (s)		$mSiO_2$-NH_2 (M)		$mSiO_2$-NH_2 (L)	
Structure	OQ_4	OQ_3	OQ_2	Q_4	Q_3	Q_4	Q_3	Q_4	Q_3
Peak intensity	15%	68%	17%	55%	45%	51%	49%	51%	49%
(OQ_3-Q_3+Q_2)				40%		37%		37%	

FE-SEM images of the as-synthesized mesoporous silica are shown in Fig. 16 and the energy dispersive spectroscopy (EDS) mapping images of mesoporous silica particles are presented in Fig. 17. The FE-SEM image shows that the morphology of particles was all different. $mSiO_2$-NH_2 (S) had amorphous shape with 1-5 um particle size. However, $mSiO_2$-NH_2 (M) and $mSiO_2$-NH_2 (L) had typical rod particle shape with high aspect ratio. Interestingly, the 1st particles aggregated each other and formed large rod type 2nd particle.

The Color mapping of $mSiO_2$-NH_2 (S) and $mSiO_2$-NH_2 (L) were performed to visualize the spatial distribution of C and N on mesoporous silica which is from APTMS. Si was colored as blue, C was visualized as red, and N was colored with yellow-green. The image shows that C and N are homogeneously dispersed on the particle and indicates that APTMS is well modified on the surface of the mesoporous silica. The particle shape and size were all different by synthesis method and surfactant.

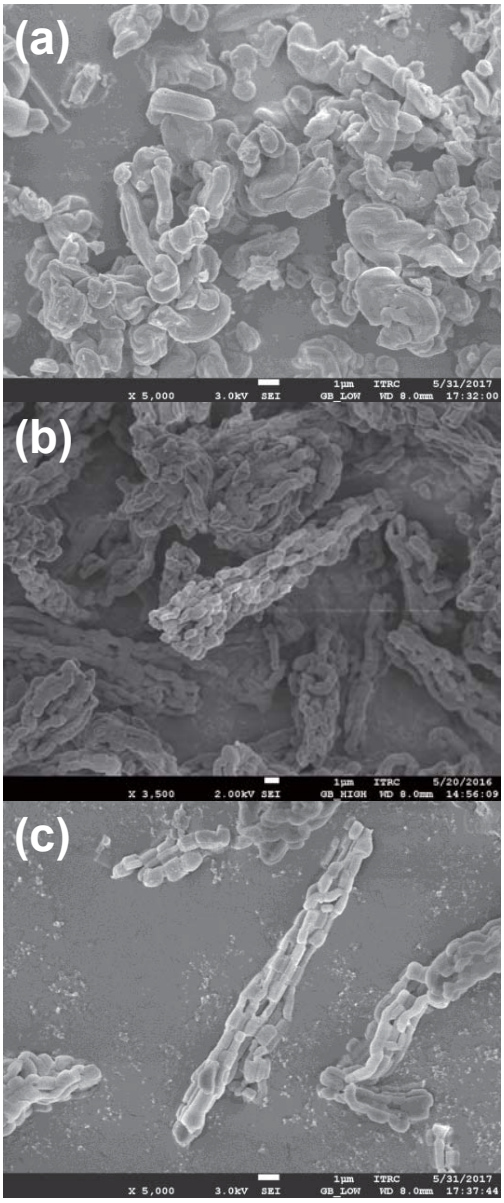

Fig. 16. Transmission electron microscope (TEM) image of functionalized mesoporous silica: (a) $mSiO_2$-NH_2 (S), (b) $mSiO_2$-NH_2 (M), (c) $mSiO_2$-NH_2 (L)

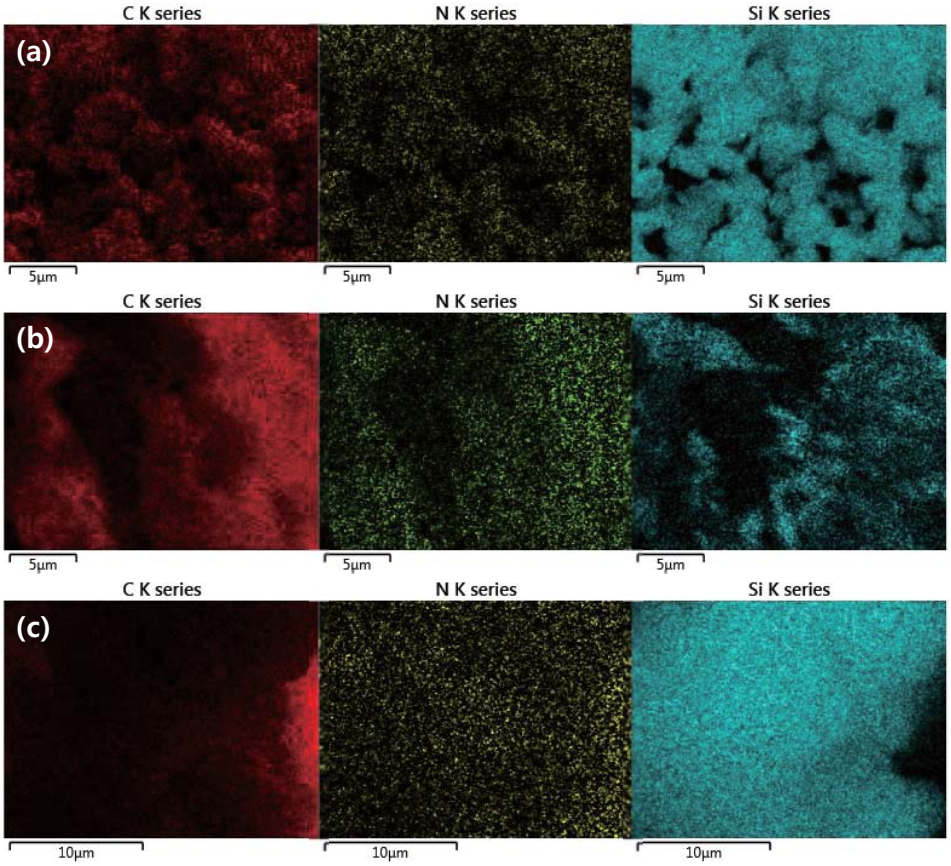

Fig. 17. Color mapping of functionalized mesoporous silica: (a) $mSiO_2$-NH_2 (S), (b) $mSiO_2$-NH_2 (M), (c) $mSiO_2$-NH_2 (L)

3.3. Evaluation of adsorption efficiency

3.3.1. Surface property effect and pore size effect

In order to investigate the surface property effect and the pore size effect of the mesoporous silica on the FFA adsorption removal efficiency, we conducted an adsorptive refining test using different mesoporous silica adsorbent at 120 °C with 5_{wt}% silica. As can be seen in Table 7, the adsorptive removal efficiency of FFA increased considerably after APTMS surface modification. All $mSiO_2$-OH samples showed FFA removal efficiency around 40% regardless of pore size difference. However, after the amine-functional group was incorporated, FFA removal efficiency of all $mSiO_2$-NH_2 samples increased to around 90%. The results indicated the amine functional group enhanced the strength of interaction between adsorbent and FFA. Besides, there was no significant effect of pore size on FFA adsorptive removal. However, in the case of chlorophyll, removal efficiency depended greatly upon pore size. The highest adsorption efficiency was shown in the pore size around 5nm, indicating the existence of an optimal pore size for chlorophyll adsorption removal.

Table 7. Adsorptive removal efficiency of FFA and chlorophyll of the mesoporous silica adsorbent

Sample	FFA removal efficiency	Chlorophyll removal efficiency
$mSiO_2$-OH (S)	44%	20%
$mSiO_2$- OH (M)	43%	48%
$mSiO_2$-OH (L)	37%	34%
$mSiO_2$-NH_2 (S)	89%	25%
$mSiO_2$- NH_2 (M)	90%	79%
$mSiO_2$- NH_2 (L)	86%	64%

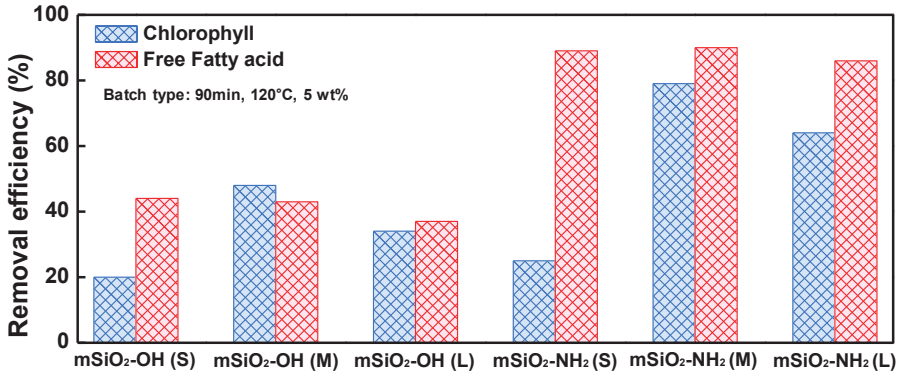

Fig. 18. Adsorptive removal efficiency of FFA and chlorophyll of the $mSiO_2$-NH_2 (M)

3.3.2. Free fatty acid adsorption kinetics

The Langmuir model successfully described the thermodynamic adsorption kinetics of FFA on mesoporous silica. As shown in Fig. 21 when X_e/q_e is plotted against X_e, a straight line with the slope of $1/Q_0$ is obtained. The correlation coefficient of both adsorbents, R^2 of 0.99 indicated that the adsorption data of FFA on the mesoporous silica adsorbent was well fitted to the Langmuir isotherm. This indicates that FFA is chemisorbed on the surface of the mesoporous silica. The values of the Langmuir isotherm constant and the monolayer capacity could be calculated from Langmuir model. Langmuir isotherm constant and maximum monolayer constant are found to increase drastically with amine functionalization. As listed in Table 8, the calculated Langmuir isotherm constant of FFA were 9.37 x 10^4 g^{-1} for $mSiO_2$-NH_2 (M) which is about 1.3 times higher than $mSiO_2$-OH (M). This result indicates that as amine functionality introduced on the surface of adsorbent, stronger bonding between FFA and adsorbent was formed. Due to stronger bonding by amine functionality maximum adsorption capacities increased drastically from 1.01 x 10^{-4} mol g^{-1} to 5.28 x 10^{-4} mol g^{-1}. The Langmuir isotherm confirmed the advantages of amine functionality on FFA removal.

The results are showing that amine functionality dramatically increased FFA adsorption efficiency. This phenomenon can be explained by the surface

amines of $mSiO_2$-NH_2 acting as specific binding sites for FFAs. We can assume that acidic proton from the FFA formed uncharged complex with amine functionality and increased the bonding strength greatly (Fig. 19). For this reason, amine functionality has selective and strong adsorption with carboxylic acid.

To verify the formation of uncharged complex of mesoporous silica with APTMS, we compared the zeta-potential of $mSiO_2$-OH (M) and $mSiO_2$-NH_2 (M) using electrophoretic light scattering (Fig. 22). The different zeta potential values effect greatly on electrokinetic interactions at the interface between adsorbate and adsorbent surfaces which result in different removal efficiency. The surface of $mSiO_2$-OH (M) has a strong negative surface charge (-47.54 mV). However, the modification of $–NH_2$ makes the strong negative charged surface turns low negative charge (-8.06 mV). The change in the surface charge resulted in great improvement of the adsorption capacity of FFA on $mSiO_2$-NH_2 (M). The results are indicating that the low negative surface charge prefers the adsorption of FFA and enhance FFA removal efficiency.

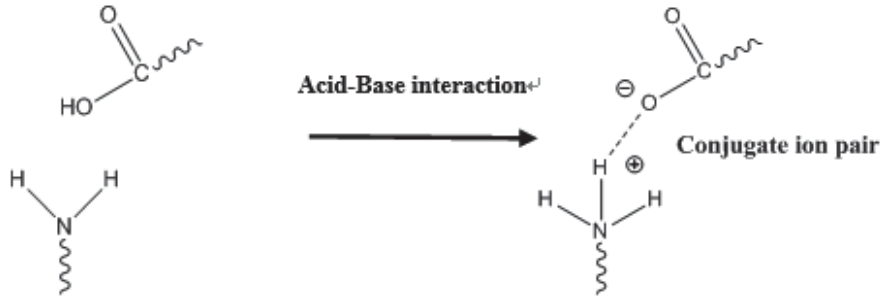

Fig. 19. Formation of uncharged complex of amine functionalized mesoporous silica

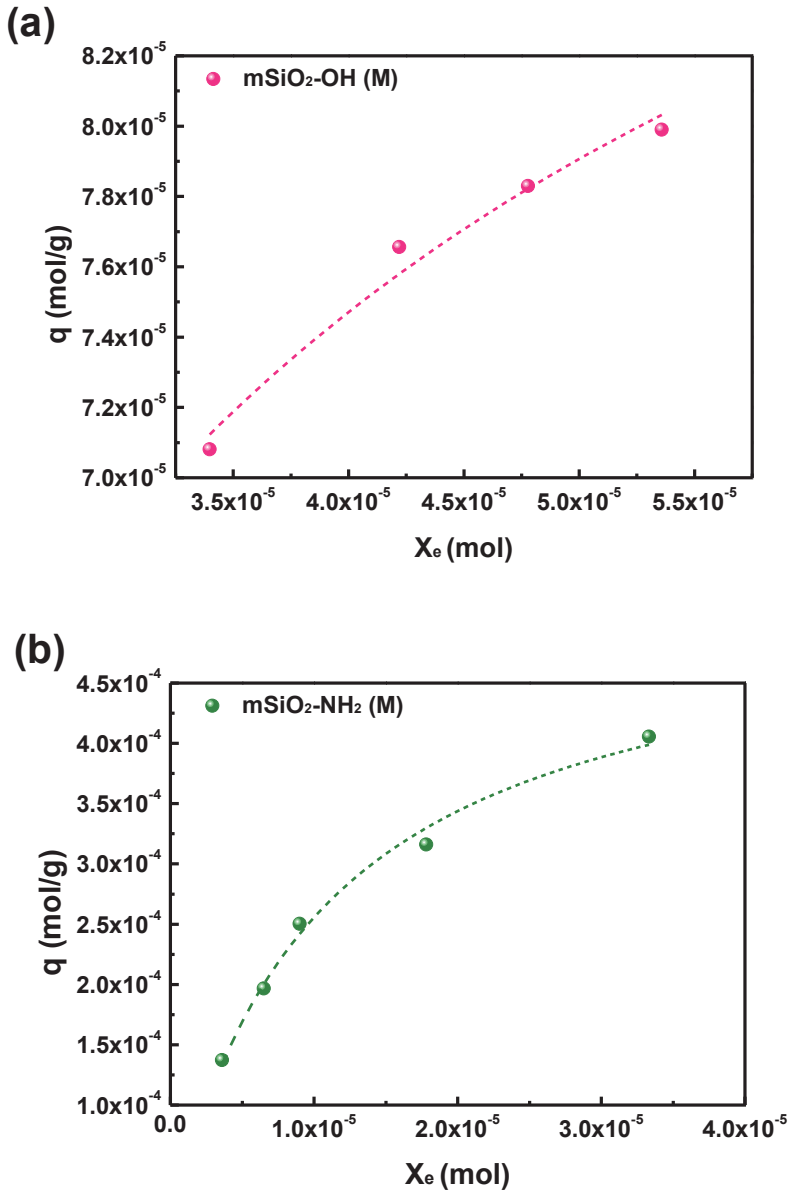

Fig. 20. Curved Langmuir adsorption model of (a) $mSiO_2$-OH and (b) $mSiO_2$-NH_2

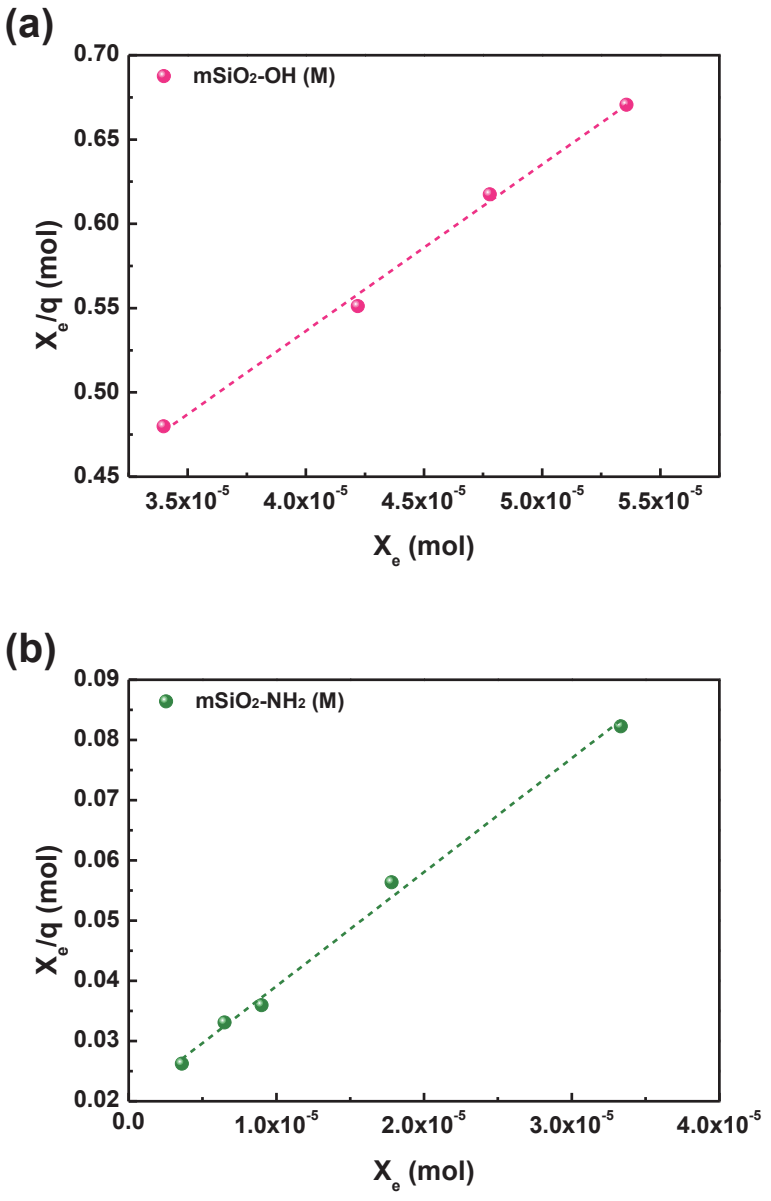

Fig. 21. Linear Langmuir adsorption model of (a) $mSiO_2$-OH and (b) $mSiO_2$-NH_2

Table 8. Langmuir constant and maximum adsorption capacity for FFA

Sample	Maximum monolayer coverage	Langmuir isotherm constant	R^2
$mSiO_2$-OH (M)	1.01 x 10^{-4} mol/g	6.97x10^4 g^{-1}	0.994
$mSiO_2$- NH_2 (M)	5.28 x 10^{-4} mol/g	9.37x10^4 g^{-1}	0.993

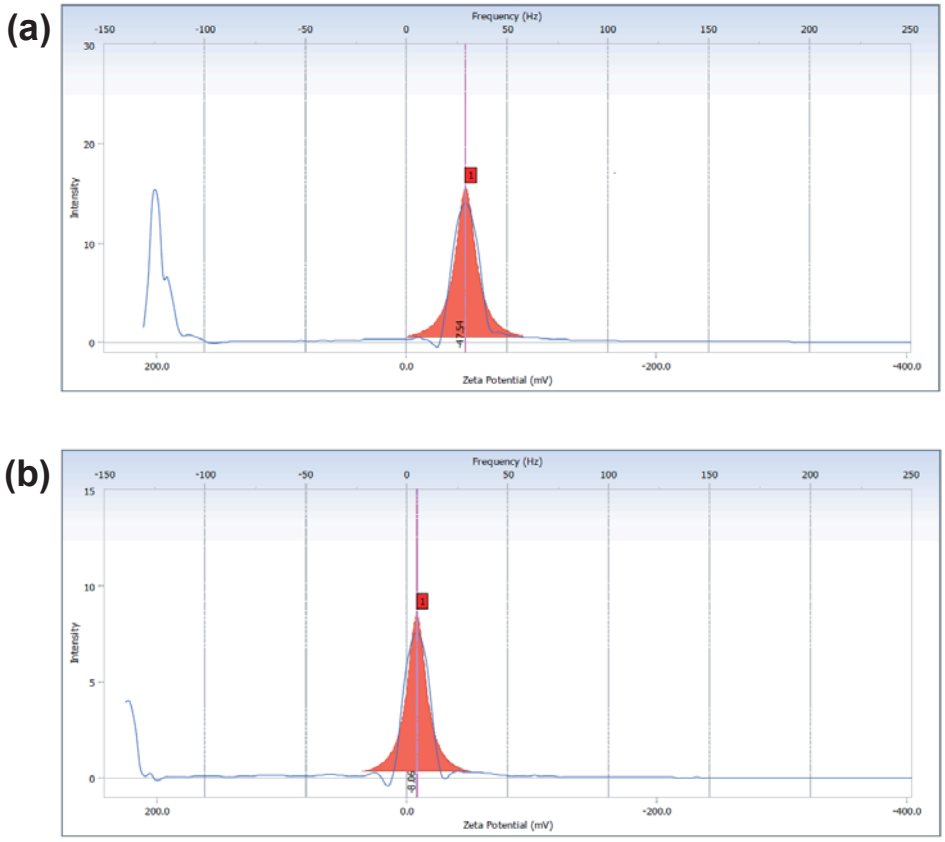

Fig. 22. Zeta potential obtained by electrophoretic light scattering of (a) $mSiO_2$-OH and (b) $mSiO_2$-NH_2

3.3.3. Chlorophyll adsorption kinetics

Fig. 23 displays the adsorption amount of chlorophyll on functionalized mesoporous silica supports as the function of time. The pore size of mesoporous silica was chosen slightly larger but still in the same order of magnitude as the dimensional size of chlorophyll. The chlorophyll adsorption on $mSiO_2$-NH_2 (M) and $mSiO_2$-NH_2 (L) reached the plateau amount rapidly in 90 min, whereas on $mSiO_2$-NH_2 (S) it underwent a gradual adsorption and reached the plateau in about 420 min. The results indicated that small pore size hindered the adsorption of chlorophyll into the porous structure and the existence of an optimal pore size for chlorophyll adsorption removal.

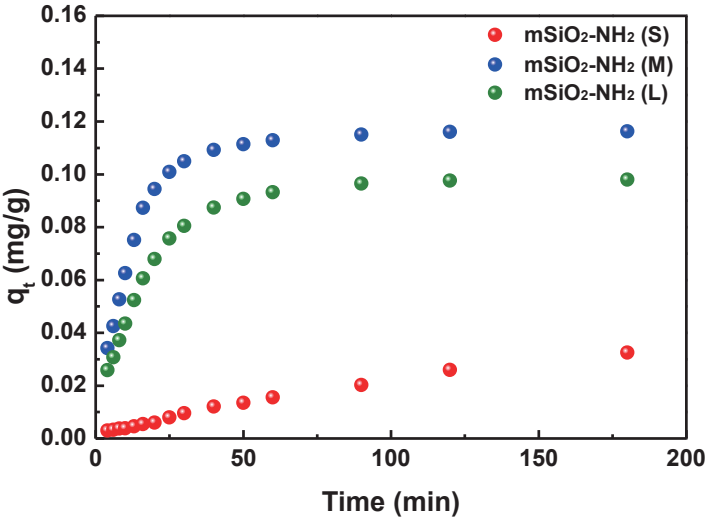

Fig. 23. Adsorption amount of chlorophyll on functionalized-ordered mesoporous silica as a function of time

The adsorption of chlorophyll is considered as a reversible reaction due to equilibrium established between two phases (liquid to solid). Pseudo-first-order kinetic model is assuming that the adsorbates are physisorbed. Therefore, Pseudo-first-order kinetic model is known for the most efficient adsorption kinetic model to examine the effect of pore size and adsorption capability of adsorbent. Maximum adsorption capacity and adsorbent rate constant could be derived from the pseudo-first-order model (Fig. 24). As listed in Table 9, the pore size of mesoporous silica had a significant effect on both theoretical maximum adsorption capacities and the adsorption rate constant of chlorophyll. The highest performance showed in the sample mSiO_2-NH_2 (M), suggesting that interaction between the silica and the chlorophyll could be optimized at this specific pore size.

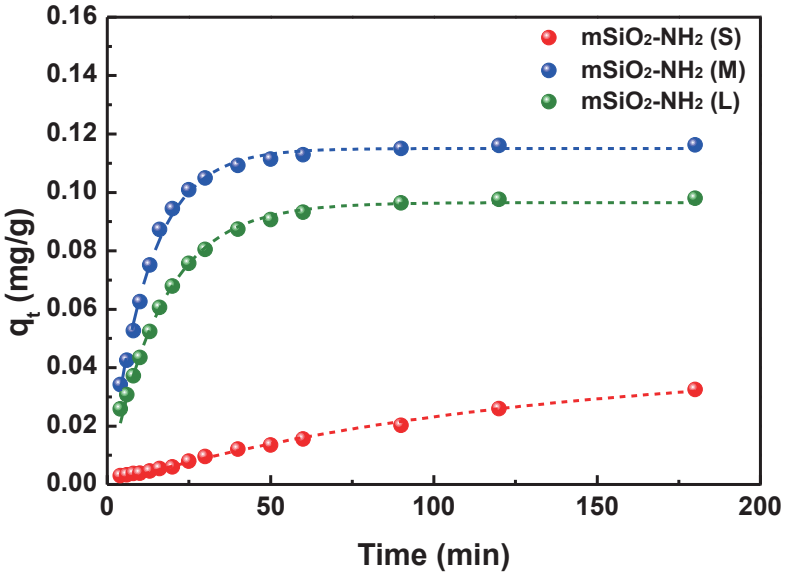

Fig. 24. Kinetic analysis of chlorophyll adsorption onto amine-functionalized ordered mesoporous silica using pseudo-first order kinetics

Table 9. Parameters of pseudo first-order kinetics of chlorophyll adsorption on $mSiO_2$-NH_2

Sample	Q_{exp} (mg g^{-1})	Q_{cal} (mg g^{-1})	k (min^{-1})	R^2
$mSiO_2$-NH_2 (S)	0.042	0.041	0.008	0.990
$mSiO_2$- NH_2 (M)	0.116	0.115	0.081	0.995
$mSiO_2$- NH_2 (L)	0.097	0.096	0.061	0.996

The apparent adsorption rate constant k_a and desorption rate constant k_d, depicting the diffusion-adsorption behavior inside the mesopores, could be investigated in detail by Poltorak model (Fig. 25). Good linear correlation is obtained in each case. From the slope and intercept, k_a and k_d could be calculated. Both k_a and k_d received significant effect by pore size as shown in Table 10. In the case of adsorption kinetic constant in pore, $mSiO_2$-NH_2 (M) had highest value. The value was 23 times higher than $mSiO_2$-NH_2 (S) and 2 times higher than $mSiO_2$-NH_2 (L). This result may be due to the pore size effect. As $mSiO_2$-NH_2 (S) has too small size for chlorophyll to freely diffuse around in the pore, the adsorption kinetic constant was low. In the case of $mSiO_2$-NH_2 (L), as pore diameter is too large to efficiently entrap chlorophyll, the kinetic constant exhibited low value.

Therefore, the adsorption kinetic constants attest that small pores restrict chlorophyll adsorption and large pores hinder strong binding with the surface. The k_a/k_d quotient is a hint of the final adsorption amount. The highest value of k_a/k_d is found for $mSiO_2$-NH_2 (M) indicating that a pore size of about 5.0 nm is the best to hold the chlorophyll inside the pores.

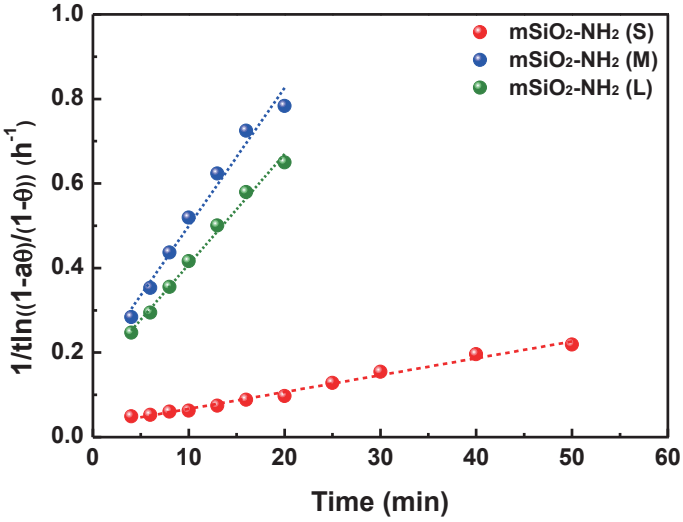

Fig. 25. Poltorak plots of chlorophyll adsorption on $mSiO_2$-NH_2

Table 10. Poltorak kinetic parameters for chlorophyll adsorption on $mSiO_2$-NH_2 Supports

Sample	K_a ($mL\ mg^{-1}min^{-1}$)	K_d (min^{-1})	K_a/K_d ($mL\ mg^{-1)}$
$mSiO_2$-NH_2 (S)	0.336	0.295	1.14
$mSiO_2$- NH_2 (M)	7.964	0..379	21.01
$mSiO_2$- NH_2 (L)	3.922	0.354	11.09

3.4. Benefits of adsorptive refining

Tocopherols are mainly used as antioxidants to prevent the oxidation of EVOO. Therefore, the concentration of tocopherols in EVOO is the critical parameter that determines the quality of the oil. However, due to the low thermal stability of tocopherol, the concentration of tocopherol drastically decreases while de-acidification process. By utilizing adsorptive refining system, we expected thermal degradation issue could be solved. HPLC analysis was taken to determine whether mesoporous silica interacts with tocopherol. The concentration of tocopherol obtained by HPLC was 334 ppm for extra virgin olive oil and 329 ppm for adsorptive refined olive oil respectively. In the case of adsorptive refining, tocopherol did not degrade, unlike de-acidification process.

The effects of adsorptive refining on the β-sitosterol content in olive oil were studied in detail by HPLC. Compared to the conventional refining process, adsorptive refined olive oil showed the outstanding result in β-sitosterol remaining. Refined olive oil showed a considerable reduction in the β-sitosterol content from 1.05 to 0.66 mg/g was observed. However, adsorptive refined olive oil showed that β-sitosterol content decreased only 0.18 mg/g than EVOO and remained in much higher ratio than refined olive oil.

The quality of the olive oil also can be examined by measuring the characteristics of the absorption bands between 200 and 300 nm. These absorbance bands are related to conjugated diene and triene systems. Low absorption in this region caused by oxidation is indicative of a high-quality olive oil. Generally, conjugated diene and triene are quantitatively expressed by Delta K value, which is the standards of olive oil in IOOC. Delta K value examined by UV-Vis spectrophotometer were 0.002 for extra virgin olive oil and 0.005 for adsorptive refined olive oil respectively. However, due to the harsh thermal condition of the refining process, Delta K value for refined olive oil increased to 0.012. The results indicated the harsh thermal condition of conventional refining process induced fatty acid's thermal degradation and decreased the quality of olive oil.

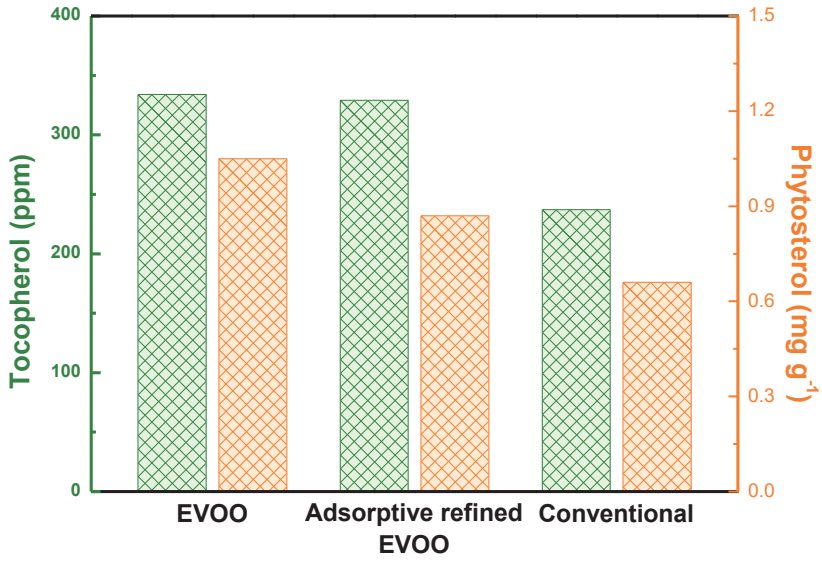

Fig. 26. Concentration of tocopherol and β-sitosterol after adsorptive removal

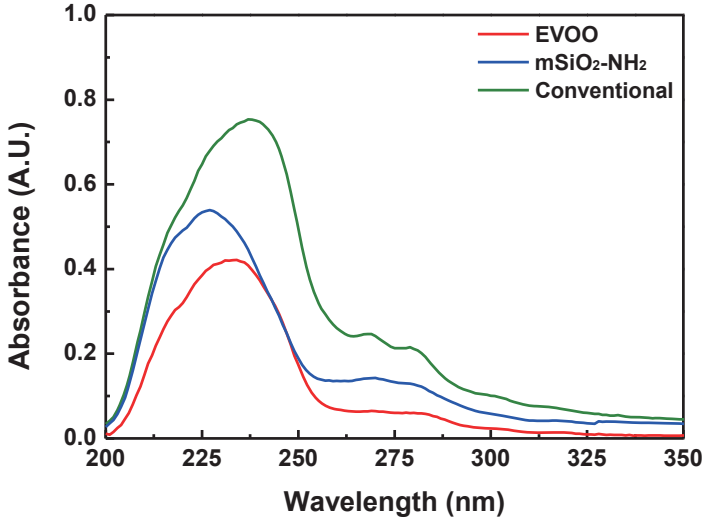

Fig. 27. UV-Vis spectra of olive oil to determine polyunsaturated ratio

3.5. Fatty acid composition of EVOO after refining

To determine the concentration of trans-unsaturated fatty acids with 18 carbon atoms that may be present in the extra virgin olive oil, gas chromatography analysis was taken. The fatty acid composition and the related sums and ratios of the 14 samples of extra virgin olive oil analyzed are summarized in Table 11. The result is showing that even after adsorptive refining by amine-functionalized mesoporous silica, the composition of fatty acid did not change. From this result, adsorptive refining using mesoporous silica can selectively remove the rancid compounds without chemical degradation. In addition all values of the fatty acid analyzed by GC, satisfied regulation of extra virgin olive oil. This result supports that adsorptive refining process has a potential to replace currently using pyro refining process.

Table 11. Fatty acid component of adsorptive refined olive oil and EVOO

	EVO	$mSiO_2$-OH (S)	$mSiO_2$-NH_2 (S)	$mSiO_2$-OH (M)	$mSiO_2$-NH_2 (M)	$mSiO_2$-OH (L)	$mSiO_2$-NH_2 (L)	Refined	Standard
C16	14.01	13.73	14.00	13.94	13.89	13.75	13.80	13.80	7.5~20
C16:1	1.18	1.15	1.19	1.17	1.18	1.15	1.16	1.16	0.3~3.5
C17	0.00	0.00	0.00	0.00	0.00	0.00	0.00	0.00	0.0~0.3
C17:1	0.00	0.00	0.00	0.00	0.00	0.00	0.00	0.00	0.0~0.3
C18	2.67	2.69	2.65	2.67	2.65	2.67	2.63	2.63	0.5~5.0
C18:1	67.84	67.80	67.35	67.67	67.61	67.61	67.26	67.26	55.0~83.0
C18:2	7.92	7.83	7.87	7.84	7.94	7.83	7.96	7.96	3.5~21.0
C18:3	0.51	0.50	0.50	0.50	0.51	0.50	0.52	0.52	0.0~0.9
C20	0.45	0.46	0.45	0.44	0.44	0.45	0.44	0.44	0.0~0.6
C20:1	0.26	0.28	0.27	0.27	0.27	0.27	0.27	0.27	0.0~0.4
C22	0.13	0.16	0.14	0.13	0.12	0.13	0.12	0.12	0.0~0.2

3.6. Column refining process

3.6.1 Breakthrough curves for rancid compounds

To investigate the potential of the column refining process, functionalized commerical mesoporous silica with a pore size of 6 nm and 15 nm were filled into their respective columns, and fixed-bed column experiment was taken. Column adsorption experiment conditions are explained in Fig. 28.

The performance of column refining is evaluated with the concept of breakthrough curve. From the breakthrough curve, the total mass of adsorbate removed by adsorbent and removal efficiency were calculated. The breakthrough curve C_t/C_0 versus breakthrough volume treated with two different mesoporous silica is shown in Fig. 29 and Fig. 30. According to the equation provided in the experimental section, removal efficiency was calculated. It was observed that the calculated q_{ed} decreased about 20% compared to the batch type adsorption. This result perhaps caused by the different adsorption condition. As the solution was not vigorously stirred in the column refining, there was less chance to adsorbate to permeate into the mesopores. Besides, unlike batch type adsorption, pore size effect was not the primary factor for removal of chlorophyll in column type adsorption.

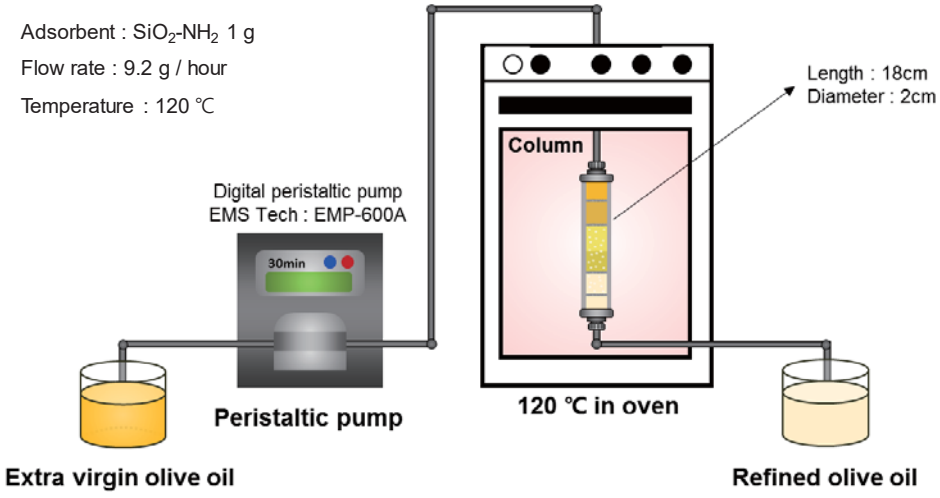

Fig. 28. Experimental set up for fixed-bed column study

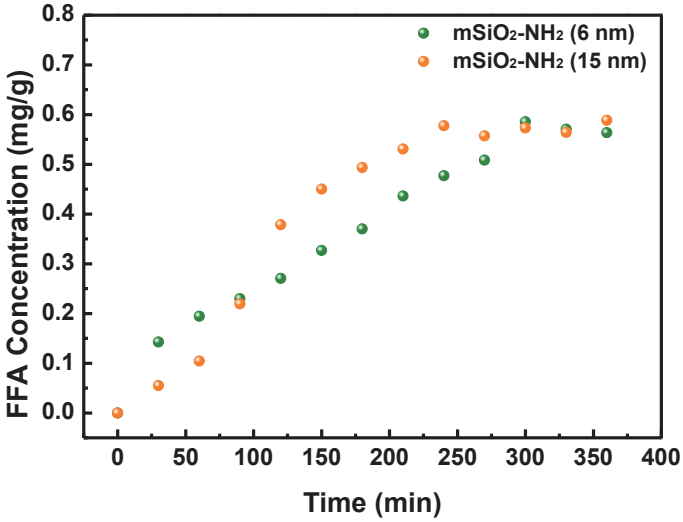

Fig. 29. Breakthrough curves for the free fatty acid

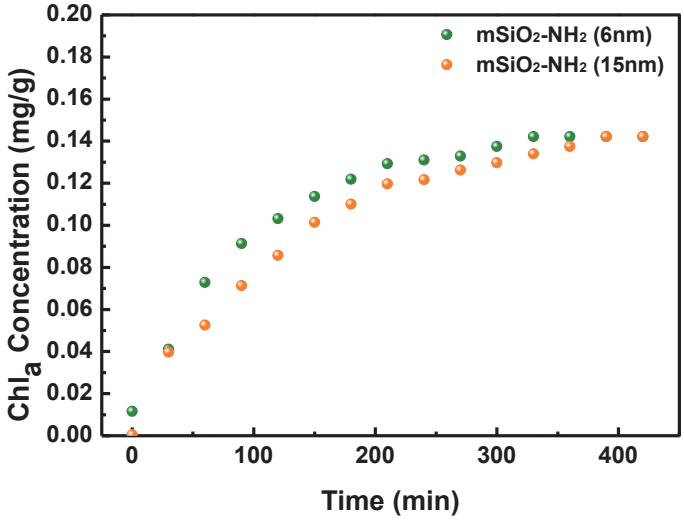

Fig. 30. Breakthrough curves for the chlorophyll

3.7. Reusability test

Commercial application of an adsorptive removal may rely deeply on the reusability of an adsorbent. For the reusability test, reusability of the $mSiO_2$-NH_2 (M) was investigated after solvent washing.

After the initial adsorptive refining of EVOO with the 5g of fresh $mSiO_2$-NH_2 (M), the used $mSiO_2$-NH_2 (M) were regenerated by washing with 500ml of several organic solvents such as toluene, acetone, and ethanol. For this, filtered used $mSiO_2$-NH_2 (M) were immersed in a solvent and kept in a sonication bath for 24 h to remove adsorbed organic molecules and residual oil. After $mSiO_2$-NH_2 (M) was washed carefully with organic solvents, the adsorbent was dried in a vacuum oven and the adsorption operations were carried out as previously described method.

As shown in Fig. 31 the regeneration efficiency of the used $mSiO_2$-NH_2 (M) after solvent washing depended deeply on the applied solvent. The performances of the regenerated $mSiO_2$-NH_2 (M), after washing with acetone, showed the 65.8% FFA removal efficiency. The reusability of $mSiO_2$-NH_2 (M) for FFA decreased on the order of acetone > ethanol > toluene washing and regeneration efficiency of each solution showed clear difference. However unlike FFA, chlorophyll removal efficiency difference was not clear as much as FFA. All three solution regenerated chlorophyll removal efficiency only

about around 25%. It seems further research about increasing chlorophyll regeneration efficiency is important.

Low regeneration efficiency of chlorophyll is due to the decreased intraparticle diffusion rate. As chlorophyll is adsorbed into the mesopore, the effective pore size is decreased which lower the intraparticle diffusion rate. Decreased intraparticle diffusion rate lowers desorption rate constant in pore as calculated by Poltorak model. This result indicates that as chlorophyll is once easily entrapped in the pore with high intraparticle diffusion rate, chlorophyll gets immobilized as pore has small free space for chlorophyll to freely move. For this reason, used adsorbent that entrapped chlorophyll is difficult to regenerate with organic solvent.

In contrast, regeneration efficiency of FFA is relatively higher than chlorophyll regeneration efficiency. This result indicate that, as FFA is small enough to freely mobilize in the pore and considerable amount of FFA is adsorbed on the outer surface of mesoporous silica.

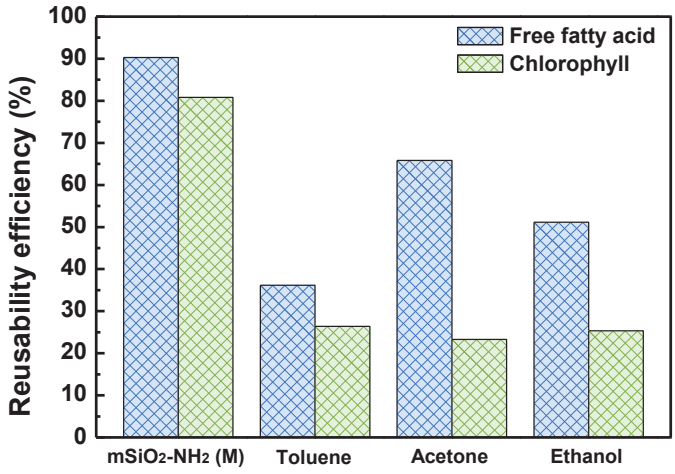

Fig. 31. Reusability test of $mSiO_2$-NH_2 (M) using solution washing

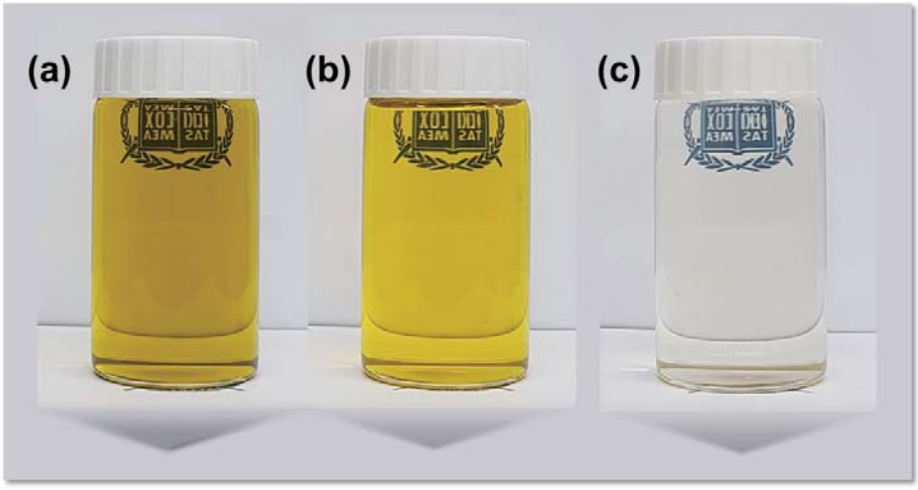

Fig. 32. Color difference of olive oil: (a) EVOO, (b) Adsorptive EVOO and (c) Conventional

4. Conclusion

We developed thermally stable EVOO by using the novel adsorptive refining process of crude olive oil to selectively remove rancid compounds. Amine functionalized mesoporous silica with a controlled pore size were readily synthesized by using various types of surfactant followed by (3-Aminopropyl)trimethoxysilane surface modification. The synthesized adsorbent removed not only FFA but also entrapped chlorophyll into the mesoporous structure with high efficiency. In particular, amine functional group drastically increased the FFA adsorption efficiency, which was systematically verified by Langmuir kinetic model. Poltorak model and pseudo-first ordered model demonstrated that the pore size with 5.8 nm exhibited superior chlorophyll adsorption capacity compared with that of 2.0 nm and 8.7 nm. In addition, mesoporous silica adsorbent removed FFA and chlorophyll selectively without removing functional compounds like tocopherol and phytosterol due to functionality and pore size effect. Therefore, $mSiO_2$-NH_2 (M) are tremendously attractive as selective, low cost, and efficient adsorbent for use in facile EVOO refining applications. We believe that our multi-functional and high-efficient adsorbent may open up a new paradigm and propose the next-generation EVOO refining process.

References

1. Tuck, Kellie L., and Peter J. Hayball. "Major phenolic compounds in olive oil: metabolism and health effects." *The Journal of nutritional biochemistry* 13.11 (2002): 636-644.
2. Owen, Robert W., et al. "Olive-oil consumption and health: the possible role of antioxidants." *The lancet oncology* 1.2 (2000): 107-112.
3. Gutfinger, T. "Polyphenols in olive oils." *Journal of the American Oil Chemists Society* 58.11 (1981): 966-968.
4. Katragadda, Harinageswara Rao, et al. "Emissions of volatile aldehydes from heated cooking oils." *Food Chemistry* 120.1 (2010): 59-65.
5. Guerrini, Lorenzo, et al. "The influence of crusher speed on extra virgin olive oil characteristics." *European Journal of Lipid Science and Technology* (2016): 34-40.
6. Miyashita, Kazuo, Naohiro Tateda, and Toru Ota. "Oxidative Stability of Free Fatty Acid Mixtures from Soybean, Linseed, and Sardine Oils in an Aqueous Solution." *Fisheries science* 60.3 (1994): 315-318.
7. Rao, Chinthalapally V., Edith Zang, and Bandaru S. Reddy. "Effect of high fat corn oil, olive oil and fish oil on phospholipid fatty acid composition in male F344 rats." *Lipids* 28.5 (1993): 441-447.

8. Sundholm, Dage. "Density functional theory calculations of the visible spectrum of chlorophyll a." *Chemical physics letters* 302.5 (1999): 480-484.

9. Weemaes, Carla A., et al. "Kinetics of chlorophyll degradation and color loss in heated broccoli juice." *Journal of Agricultural and Food Chemistry* 47.6 (1999): 2404-2409.

10. Verleyen, Tom, et al. "Influence of the vegetable oil refining process on free and esterified sterols." *Journal of the American Oil Chemists' Society* 79.10 (2002): 947-953.

11. Koris, Andras, and Gyula Vatai. "Dry degumming of vegetable oils by membrane filtration." *Desalination* 148.1 (2002): 149-153.

12. Brimberg, U. I. "Kinetics of bleaching of vegetable oils." *Journal of the American Oil Chemists' Society* 59.2 (1982): 74-78.

13. Martins, P. F., et al. "Free fatty acid separation from vegetable oil deodorizer distillate using molecular distillation process." *Separation and Purification Technology* 48.1 (2006): 78-84.

14. Wiedermann, L. H. "Degumming, refining and bleaching soybean oil." *Journal of the American Oil Chemists' Society* 58.3 (1981): 159-166.

15. Bucci, Remo, et al. "Chemical authentication of extra virgin olive oil

varieties by supervised chemometric procedures." *Journal of agricultural and food chemistry* 50.3 (2002): 413-418.

16. Bhosle, B. M., and R. Subramanian. "New approaches in deacidification of edible oils—a review." *Journal of Food Engineering* 69.4 (2005): 481-494.

17. Kobya, M., et al. "Adsorption of heavy metal ions from aqueous solutions by activated carbon prepared from apricot stone." *Bioresource technology* 96.13 (2005): 1518-1521.

18. Aguado, José, et al. "Aqueous heavy metals removal by adsorption on amine-functionalized mesoporous silica." *Journal of Hazardous Materials* 163.1 (2009): 213-221.

19. Demirbas, Ayhan. "Heavy metal adsorption onto agro-based waste materials: a review." *Journal of hazardous materials* 157.2 (2008): 220-229.

20. Yu, Bin, et al. "The removal of heavy metal from aqueous solutions by sawdust adsorption—removal of copper." *Journal of Hazardous Materials* 80.1 (2000): 33-42.

21. Bibby, Ashley, and Louis Mercier. "Mercury (II) ion adsorption behavior in thiol-functionalized mesoporous silica microspheres." *Chemistry of*

materials 14.4 (2002): 1591-1597.

22. Lu, Shan, Zhihong Song, and Jing He. "Diffusion-controlled protein adsorption in mesoporous silica." *The Journal of Physical Chemistry B* 115.24 (2011): 7744-7750.

23. Bui, Tung Xuan, and Heechul Choi. "Adsorptive removal of selected pharmaceuticals by mesoporous silica SBA-15." *Journal of Hazardous Materials* 168.2 (2009): 602-608.

24. Manzano, M., et al. "Studies on MCM-41 mesoporous silica for drug delivery: effect of particle morphology and amine functionalization." *Chemical Engineering Journal* 137.1 (2008): 30-37.

25. Kresge, C. T., et al. "Ordered mesoporous molecular sieves synthesized by a liquid-crystal template mechanism." *nature* 359.6397 (1992): 710-712.

26. Zhao, Dongyuan, et al. "Morphological control of highly ordered mesoporous silica SBA-15." *Chemistry of Materials* 12.2 (2000): 275-279.

27. Wang, Ye, et al. "Synthesis of SBA-15 with different pore sizes and the utilization as supports of high loading of cobalt catalysts." *Catalysis Today*68.1 (2001): 3-9.

28. Song, S-W., K. Hidajat, and S. Kawi. "Functionalized SBA-15 materials as carriers for controlled drug delivery: influence of surface properties on matrix-drug interactions." *Langmuir* 21.21 (2005): 9568-9575.

29. Foo, 5. 5. K., Hameed, B. H., et al. “Insights into the modeling of adsorption isotherm systems.” *Chemical Engineering Journal* 156.1 (2010): 2-10.

30. Wu, Feng-Chin, et al. "Characteristics of pseudo-second-order kinetic model for liquid-phase adsorption: A mini-review." *Chemical Engineering Journal* 151.1 (2009): 1-9.

31. Lyubinskii, G. V., and V. A. Tertykh. "Influence of chemical nature of surface and geometrical characteristics of silica matrices on immobilization of proteins." *Theoretical and Experimental Chemistry* 26.2 (1990): 185-192.

32. Xu, Xing, et al. "Nitrate adsorption by stratified wheat straw resin in lab-scale columns." *Chemical engineering journal* 226 (2013): 1-6

국문 초록

우리 인체에 유익한 영양성분은 유지하면서 유리지방산과 엽록소를 선택적으로 제거하는 것은 고온조리가 가능한 엑스트라 버진 올리브유 생산에 있어서 필수적이다. 이번 연구에서 우리는, 기공 크기가 조절된 그리고 (3-Aminopropyl)trimethoxysilane 으로 기능화된 메조 기공 실리카를 사용하여 산패입자를 선택적으로 제거함으로써 EVOO의 열적 안정성을 증가 시켰다. 메조 기공 실리카에 대한 산패입자들의 흡착 거동은 Langmuir 흡착모델, pseudo-first 속도론 그리고 Poltorak 모델을 활용하여 정량적으로 분석하였다. 가장 높은 엽록소 흡착 효율은 기공크기 5.85 nm 에서 나타났으며, 이는 메조기공 실리카와 엽록소 사이의 상호작용은 특정 기공 크기에서 최적화 될 수 있음을 암시한다. 특히 아민기로 기능화 된 메조기공 실리카는, 개질 되지 않은 메조기공 실리카와 비교하여 FFA 흡착 효율이 현저하게 개선되었다. 또한 토코페롤 및 식물성 스테롤과 같은 EVOO 속 유익한 영양성분들은 흡착 정제 이후에도 유지됨을 확인하였다. 이 결과를 토대로 기공 크기가 조절되고 아민기로 개질된 메조 기공 실리카를 활용한 엑스트라 버진 올리브유 정제공정은 큰 관심을 끌 것으로 기대된다.